JOURNAL OF GEOPHYSICAL RESEARCH, VOL. 113, A06308, doi:10.1029/2007JA012999, 2008

Combined EISCAT radar and optical multispectral and tomographic observations of black aurora

B. Gustavsson,[1] M. J. Kosch,[2] A. Senior,[2] A. J. Kavanagh,[2] B. U. E. Brändström,[3]
and E. M. Blixt[1]

Received 19 December 2007; revised 6 February 2008; accepted 25 February 2008; published 25 June 2008.

[1] Black auroras are recognized as spatially well-defined regions within a uniform diffuse auroral background where the optical emission is significantly reduced. Black auroras typically appear post-magnetic midnight and during the substorm recovery phase, but not exclusively so. We report on the first combined multimonochromatic optical imaging, bistatic white-light TV recordings and incoherent scatter radar observations of black aurora by EISCAT of the phenomenon. From the relatively larger reduction in luminosity at 4278 Å than at 8446 Å we show that nonsheared black auroras are most probably not caused by downward directed electrical fields at low altitude. From the observations, we determine this by relating the height and intensity of the black aurora to precipitating particle energy within the surrounding background diffuse aurora. The observations are more consistent with an energy selective loss cone. Hence the mechanism causing black aurora is most probably active in the magnetosphere rather than close to Earth.

Citation: Gustavsson, B., M. J. Kosch, A. Senior, A. J. Kavanagh, B. U. E. Brändström, and E. M. Blixt (2008), Combined EISCAT radar and optical multispectral and tomographic observations of black aurora, *J. Geophys. Res.*, *113*, A06308, doi:10.1029/2007JA012999.

1. Introduction

[2] Black aurorae are structures within diffuse aurora with lower luminosity [*Oguti*, 1975; *Royrvik*, 1976]. They can either appear as small patches or black rings that drift, mainly eastward, or thin black arcs with or without distinct shear motion [*Trondsen and Cogger*, 1997; *Kimball and Hallinan*, 1998a, 1998b]. Their main features can be summarized [e.g., *Trondsen and Cogger*, 1997; *Kosch et al.*, 1998b] as follows: Black auroras are mostly east-west aligned arc segments or patches, with a typical size of 0.5–1.5 × 2.5–5 (up to 20) km. They normally occur postsubstorm, typically in a diffuse aurora background, and drift eastward postmagnetic midnight with a typical velocity of 0.5–1.5 (up to 4) km/s. They may exhibit shear or vortices. In many respects, the black aurorae are analogous to the negative of normal aurora [*Trondsen and Cogger*, 1997]. Hence just like normal aurora, the different morphologies of the black aurora (e.g., sheared forms showing vorticity versus unsheared forms) may be due to different mechanisms.

[3] The classical understanding of black aurora, built on FREJA satellite data by *Marklund et al.* [1997, 1994], is that the reduction in emission is caused by a downward electrical field that drives a downward current. This we will denote "the retarding potential model". At auroral latitudes, in the altitude range between 800 and 1700 km, there are narrow structures (down to ≈ 1–2 km) with diverging electric fields (up to ≈ 1–2 V/m), dropouts of precipitating electrons, and depletions of thermal plasma. Although no simultaneous optical observations were available to confirm the presence of black auroras, this is associated with black curls and black arcs with sheared flow that have been observed by, for example, *Royrvik* [1976] and *Kimball and Hallinan* [1998b].

[4] On the other hand, joint aircraft-based optical and FAST satellite observations by *Peticolas et al.* [2002] indicate inhibition of pitch angle scattering of magnetospheric particles into the loss cone as the cause of the black structures. The FAST observations show narrow 50% bite-outs in downward electron energy flux above regions with diffuse aurora, where only the flux above 3–4 keV inside the downward going loss cone is decreased while the electron fluxes at other pitch angles are identical inside and outside the bite-out region. *Peticolas et al.* [2002] describe the electron spectra as a "partial double loss cone" and we will refer to this mechanism as such.

[5] Combined radar and optical observations of quiet black nonsheared arcs [*Blixt and Kosch*, 2004] indicate that they are not colocated with any detectable downward current. Furthermore, the drift velocity of black patches has no clear relationship to the ionospheric convection [*Schoute-Vanneck et al.*, 1990; *Blixt et al.*, 2005b], but rather correlates with the energy of the precipitating electrons in the surrounding diffuse aurora [*Blixt et al.*, 2005b].

---

[1] Department of Physics and Technology, University of Tromsø, Tromsø, Norway.

[2] Department of Communication Systems, Lancaster University, Lancaster, UK.

[3] Kiruna Division, Swedish Institute of Space Physics, Kiruna, Sweden.

0148-0227/08/2007JA012999$09.00

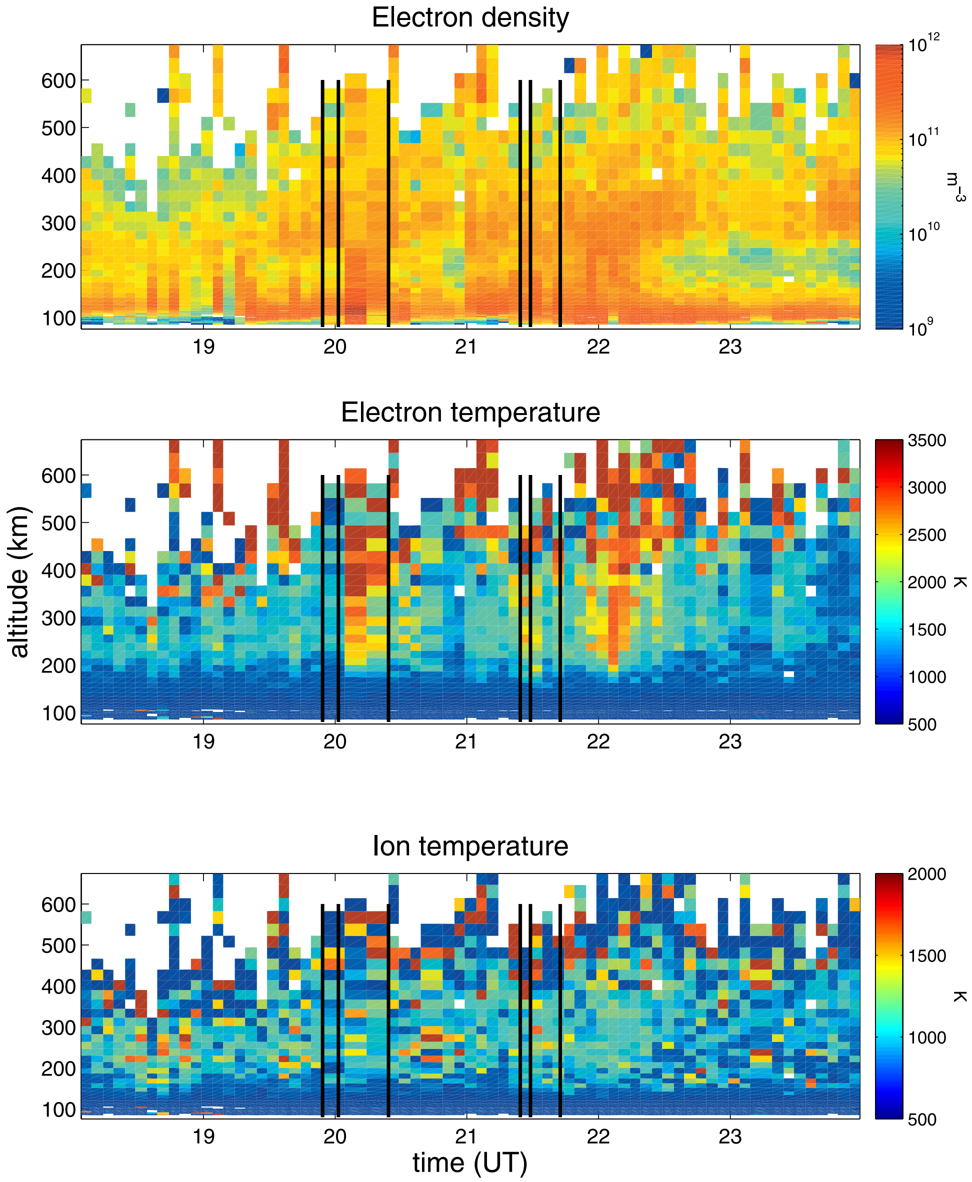

Figure 1. EISCAT UHF IS observations of electron density (top), electron temperature (middle), and ion temperature (bottom). For the time periods marked with black vertical lines the radar was pointing into magnetic zenith simultaneously with optical observations of black aurora.

This is not consistent with a mechanism acting at low altitudes following the ionospheric convection. The correlation between the electron energy and the drift of black aurora agrees better with a mechanism acting in the equatorial plane, codrifting with the curvature and gradient drift of trapped energetic electrons. However, there are yet no simultaneous optical and satellite observations confirming this.

[6] It is also worth noting that in diffuse aurora a typical sequence of events is the appearance of black patches (possibly followed by black rings [*Kimball and Hallinan*, 1998a]), that extends to, or is followed by, east-west aligned black arcs [*Royrvik*, 1976; *Trondsen and Cogger*, 1997] that might develop shear flow and create black curls, followed by the discrete aurora surrounding the black arcs intensifying and becoming "normal" discrete arcs. This sequence can repeat several times.

[7] In this paper we present simultaneous multimonochromatic and white-light bistatic optical observations as well as incoherent scatter (IS) radar observations of the diffuse and black aurora. The IS observations were made with the European Incoherent Scatter (EISCAT) UHF radar, located near Tromsø Norway, [*Rishbeth and van Eyken*, 1993; *Turunen et al.*, 2002] and gives estimates of electron concentration as well as electron and ion temperatures. From these we obtain estimates of the energy spectra of the precipitating electrons. The white-light bistatic imaging, using the Digital All-Sky Imager (DASI) [*Kosch et al.*, 1998a] located at the EISCAT site and the Odin imager [*Blixt et al.*, 2005a] located 27 km away, is used to validate the estimate of the electron spectra by tomographic inversion methods of the optical data. The multiwavelength optical observations were obtained with the Auroral Large Imaging System (ALIS) [*Brändström*, 2003] station in

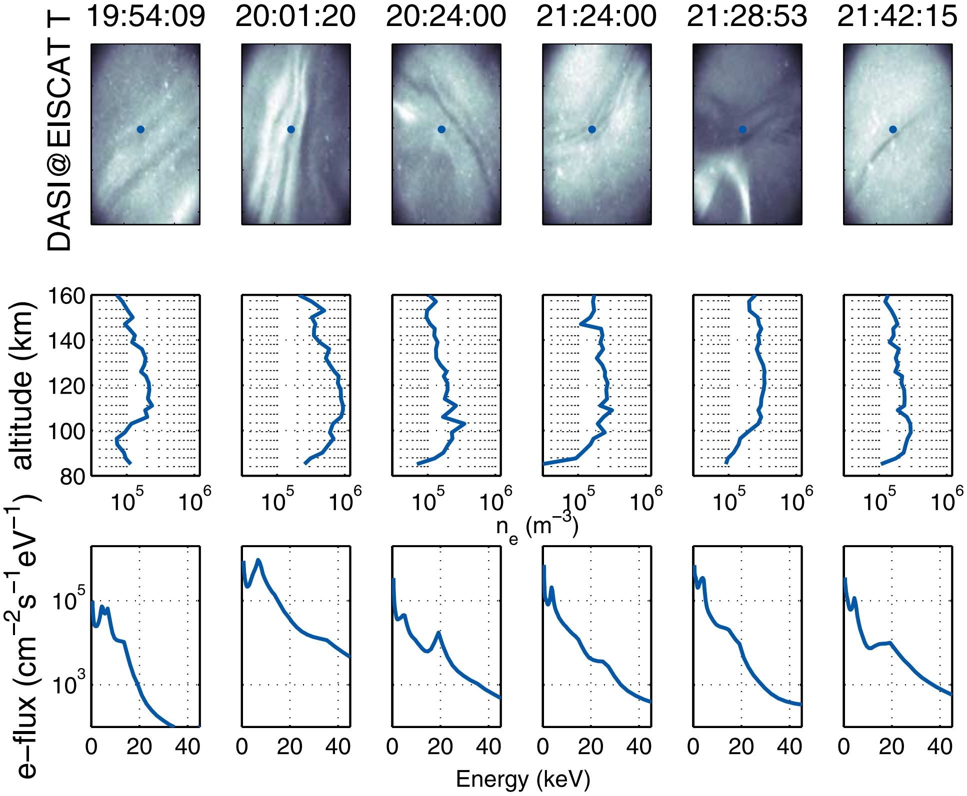

Figure 2. Data from the 8 October 2005 campaign taken at Troms, Norway. The top row shows white-light optical data from DASI with a ≈30° field of view, clearly showing evidence of black auroras. The blue dot indicates the EISCAT UHF radar pointing direction along the magnetic field direction. The middle row shows the electron density profile from EISCAT. The bottom row of panels show the precipitating particle energy spectrum, inferred from inverting the EISCAT data.

Skibotn which was switching between filters for 4278, 8446, and 5577 Å between exposures. These observations provide us with quantitative column emission rates in both the diffuse aurora and in the black aurora for two prompt emissions, 4278 and 8446 Å, that are only excited by direct electron impact. Since these emissions respond differently to the energy of electron precipitation, we use them to test the two theories of black aurora taking the precipitating electron spectrum determined from the EISCAT observations as a reference.

2. Observations

[8] On 8 October 2005, the DASI TV imager was located at the EISCAT radar site (69.59°N, 19.23°E), recording in white-light with a ≈30° field of view and pointing into the magnetic zenith (12.8°S). The ODIN TV imager was located 21.76 km to the south and 16.22 km to the east, also recording in white-light with a 15 × 11° field of view and pointing into the common volume, giving overlapping fields-of-view from D-region altitudes and above. The EISCAT UHF radar was performing a 7-position scan for an unrelated purpose, pointing into the magnetic zenith once every 5 min, measuring electron density and electron and ion temperature, as shown in Figure 1. The ALIS imager in Skibotn (69.35°N, 20.36°E), with a 90° field-of-view observed in the zenith, with a filter cycle of 4278, 5577, 4278, 8446 Å with 1.6 s exposure time and 4 s between exposures. Black auroras were observed in the interval 20–22 UT.

[9] Figure 2 (top) shows optical data from DASI of unsheared black auroras. The blue dot indicates the EISCAT UHF radar pointing direction along the magnetic field direction. Figure 2 (middle row of panels) shows the corresponding electron density profile from EISCAT. Figure 2 (bottom) shows the precipitating particle energy spectrum, retrieved from the EISCAT data. The inversion algorithm employed was the maximum entropy inversion developed by *Semeter and Kamalabadi* [2005]. Unfortunately, due to the scanning pattern of the radar, we could not make the correction for temporal variations of the electron concentration. However, for the comparatively slowly varying diffuse aurora this should not be a major concern.

[10] The energy spectra of the precipitating electrons was estimated from the electron density profiles for the times when EISCAT observed in magnetic zenith simultaneously with optical observations of the black aurora, marked in Figure 1. The estimates of the electron spectra are best characterized as multipeaked distributions with maxima around a few keV, as is shown in Figure 2. Furthermore, the high energy tails are fairly wide, up to several tens of keV.

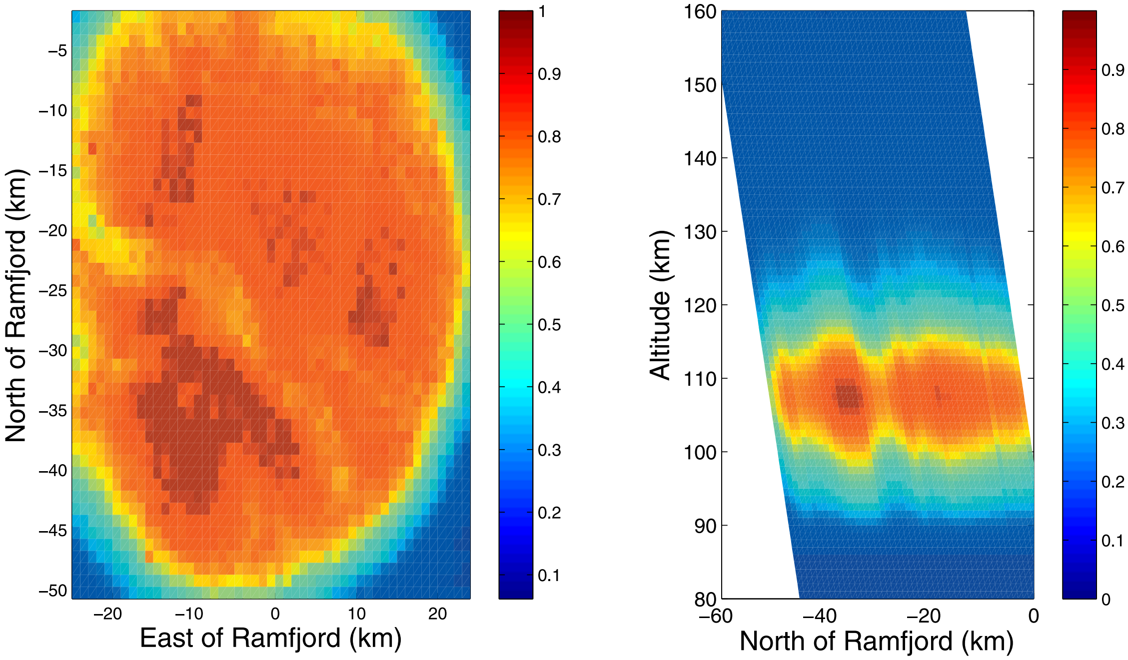

Figure 3. Cuts through the estimated three-dimensional distribution of diffuse auroral volume emission rates at 2023:48 UT, in arbitrary intensity units. In the left a horizontal cut at 108 km of altitude and in the right a meridional slice through Ramfjord is shown.

[11] The estimate of the electron spectra from EISCAT data is validated by comparing the bistatic white-light images with calculated images from a modeled three-dimensional distribution of volume emission rates, where the altitude variation is proportional to the energy deposition of the electron spectra, and the horizontal variation in column emission rate is taken proportional to the DASI images from Ramfjord projected to the altitude of maximum volume emission rate (108 km) as shown in Figure 3, which is consistent with the 115 km *Peticolas et al.* [2002] calculated from FAST electron data. This three-dimensional volume emission distribution is then used to calculate the spatial intensity variation DASI and Odin would observe. Figure 4 shows the comparison between observed images, shown in the left column, and the modeled images, shown in the right column, in arbitrary intensity units. In the top row the fit for the DASI imager located at the EISCAT site is good, which is unsurprising since that observed image was used for the horizontal intensity variation. In the bottom row the fit for the Odin imager, located 27 km to the south-east, is also good, which verifies the retrieval of the electron energy spectra.

[12] Simultaneously with the observations in the Ramfjord area the same diffuse (and black aurora) was observed by the Auroral Large Imaging System (ALIS) [*Brändström*, 2003] station in Skibotn (69.35°N, 20.36°E, 45 km east and 28 km south of the EISCAT site) in 5577, 4278, and 8446 Å. Figures 5 and 6 shows images in calibrated intensity units at selected times, which show regions with reduced column emission rates, in both in 4278 Å from N_2^+ ,and in 8446 from O(3p^3P). For the events we have selected here (two shown here and an additional three events during the same time period) the dark structures were close to magnetic zenith for a period of time that covered two exposures at 4278 Å and one at 8446 Å in-between, thus we can rule out perspective effects and temporal variations as cause to smearing of the structures. Near-meridional intensity cuts show the absolute intensity variation in the diffuse background aurora, and in the black aurora. The black aurora corresponds to a reduction from 2100–2500 Rayleighs to approximately 1600–1800 R in 4278 Å, while in 8446 Å the reduction is from 1700–1900 R to 1400–1600 R. In both cases, the reduction in optical intensity is not even half of the intensity of the surrounding diffuse aurora. For the first time, we provide quantitative optical evidence that the black aurora are not entirely devoid of optical emissions. Their visually black appearance, and hence their name, is an artifact of human vision and low contrast night-vision TV systems.

3. Analysis

[13] The way the primary spectra of the precipitating electrons in the diffuse aurora is modified to cause the black aurora differs for the two theories. For the retarding-potential model, the downward directed electric field will reduce the energy of all electrons, and reflect electrons with energies lower than the retarding potential, ΔE. For the partial-double-loss cone model, the flux for energies above the cut-off energy, E_{cut}, will be reduced. As we have estimates of the primary electron spectra for the regions of diffuse aurora, we can calculate the altitude-energy variation of electron flux for varying model parameters ΔE and E_{cut} for the two theories. Since both the 4278 and 8446 Å emissions are prompt and produced by direct electron impact, these electron fluxes will directly give us the

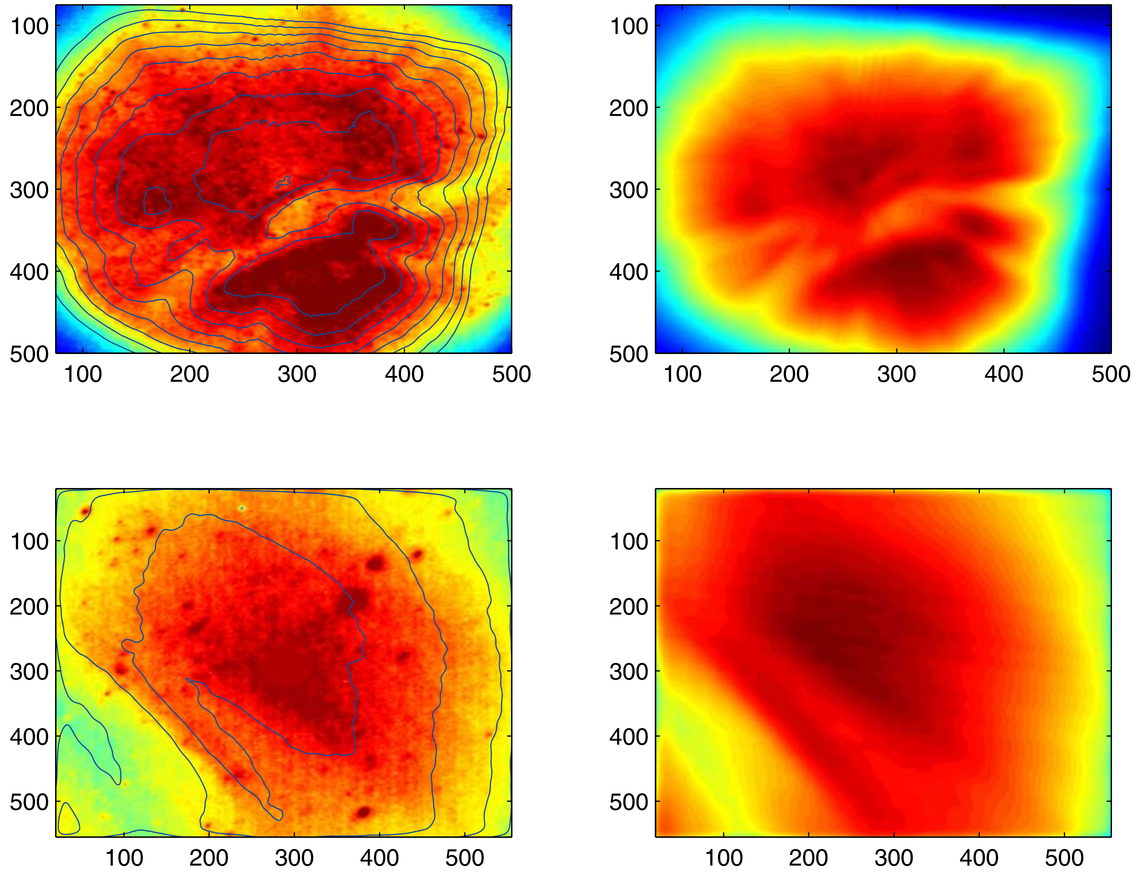

Figure 4. Comparison between observed images for 2023:48 UT, shown in the left column, and the modeled images, shown in the right column, in arbitrary intensity units. The contours overlaid in the left column are isointensity contours for the modeled images. The top row contains the DASI observation and modeled projection from Ramfjord and the bottom row the observation and modeled projection for ODIN.

variation at 4278 and 8446 Å as a function of the model parameters. The production rate for the two optical emissions responds differently to particle precipitation of different energy, partly because the emission cross-sections vary differently with energy but mainly because of the different scale heights of N_2 and O, as can be seen in Figure 7. Hence comparing the modeled and observed optical intensities is a direct test for the two theories of the black aurora.

[14] For the diffuse aurora the precipitating electrons have an isotropic pitch angle distribution [e.g., *Peticolas et al.*, 2002], thus, we calculate the production rates by solving the electron transport equation for downward, I^d, and upward, I^u, electron fluxes:

$$\bar{\mu}\frac{\partial I^u}{\partial s} = -AI^u(E,s) + n_e(s)\frac{\partial}{\partial E}[L(E)I^u(E,s)] + BI^d(E,s) + C^u(E,s) + Q(E,s)/2 \quad (1)$$

$$-\bar{\mu}\frac{\partial I^d}{\partial s} = -AI^d(E,s) + n_e(s)\frac{\partial}{\partial E}\left[L(E)I^d(E,s)\right] + BI^u(E,s) + C^d(E,s) + Q(E,s)/2 \quad (2)$$

Here s is the distance along the magnetic field, which has a 12.8° inclination at Tromsø, and $\bar{\mu}$ is the pitch angle cosine average, for which we use $1/\sqrt{3}$ [e.g., *Stamnes*, 1981; *Solomon et al.*, 1988]. The first term represents losses due to elastic scattering to flux in the opposite direction and energy degradation caused by inelastic scattering with

$$A = \sum_k n_k(s)\left(\rho_e^k(E)\sigma_e^k(E) + \rho_i^k(E)\sigma_i^k(E)\right)$$

where $n_k(s)$ is the concentration of the k-th neutral species, for which we use the MSIS model atmosphere [*Hedin*, 1991], and $\rho^k(E)$, $\sigma_e^k(E)$ and $\sigma_i^k(E)$ are the backscatter ratio, the elastic cross section and the total inelastic cross section at electron energy E for collisions with the k-th species.

[15] The second term represents the losses due to energy transfer to the ambient electrons [*Swartz et al.*, 1971]:

$$L(E) = \frac{3.37 \cdot 10^{-12}}{E^{0.94} n_e^{0.03}}\left(\frac{E - E'}{E - 0.53E'}\right)^{2.36}$$

where n_e is the ambient electron concentration and $E' = k_B T_e$ is the thermal electron energy in *eV*. The third term

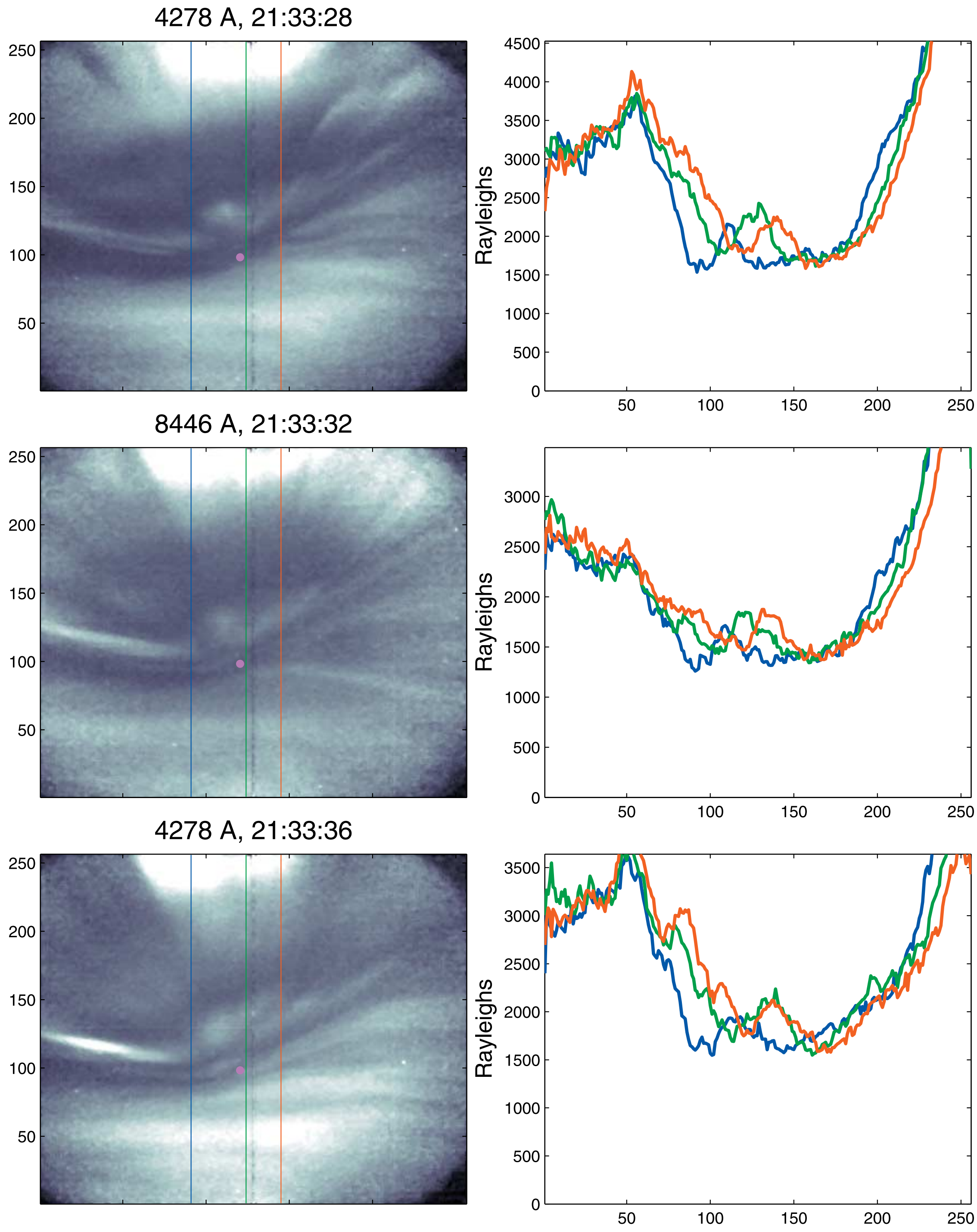

Figure 5. Left column shows consecutive images in 4278, 8446, and 4278 Å taken with 4 s interval from 21:33:28 to 21:33:36 UT on 8 October 2008. In the right column the color-coded near-meridional cuts, marked in the left, show the absolute intensity variation in the diffuse and black auroras. The red dot marks magnetic zenith.

represents the contribution from elastic scattering from the flux in the opposite direction with:

$$B = \sum_k n_k(s)\rho^k(E)\sigma_e^k(E)$$

The fourth term represents a flux source by cascading from higher energies, ϵ, where

$$C^{u,d} = \sum_k n_k(s)\sum_i \int_{E_j}^{E_j+\delta E} \sigma_i^k(\epsilon)\left[(1-\rho_i^k(\epsilon))I^{u,d}(\epsilon,s) + \rho_i^k(\epsilon)I^{d,u}(\epsilon,s)\right]dE$$

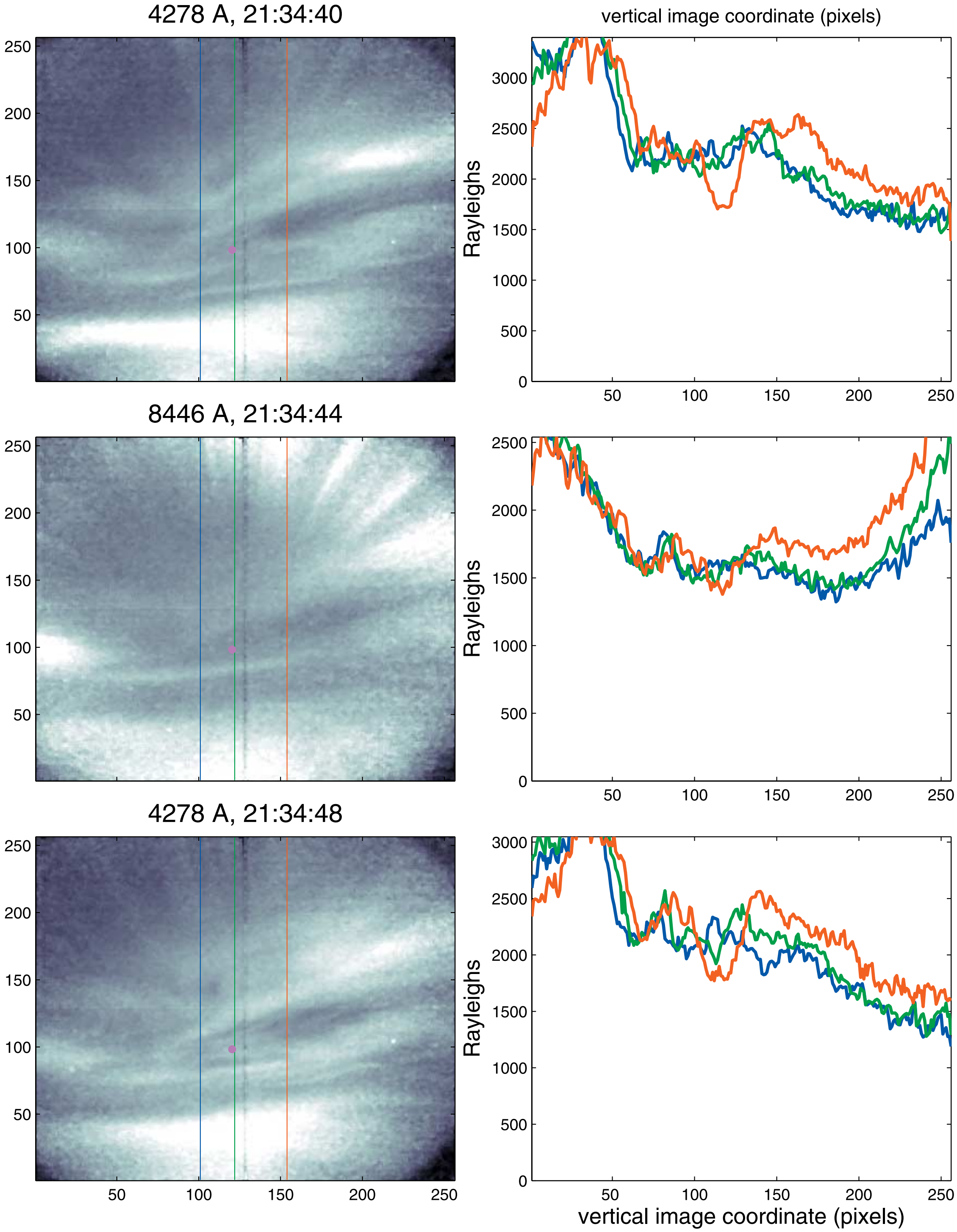

Figure 6. Same as Figure 5, but for the time period from 21:34:40 to 21:34:48 UT.

Here $\epsilon = E+W_i$, where W_i is the electron energy loss to excitation (and ionization) of state i, σ_i^k is the inelastic cross section for electrons with energy ϵ. To conserve energy and the total number of electrons in collisions, we take into account the width δE of the energy interval between E_j and E_{j+1} when calculating both A and C by using a modified version of the discrete wide energy bin method [e.g., *Porter et al.*, 1987]. For ionization the degraded primary electrons are distributed over energies E such that $E = E_i - W_i + E_s$ where E_s is the energy of secondary electrons. The source Q represents the internal source of secondary electrons from ionization, which we assume contributes equally to both the upward and downward fluxes. Here we use the differential cross sections for production of secondary electrons from

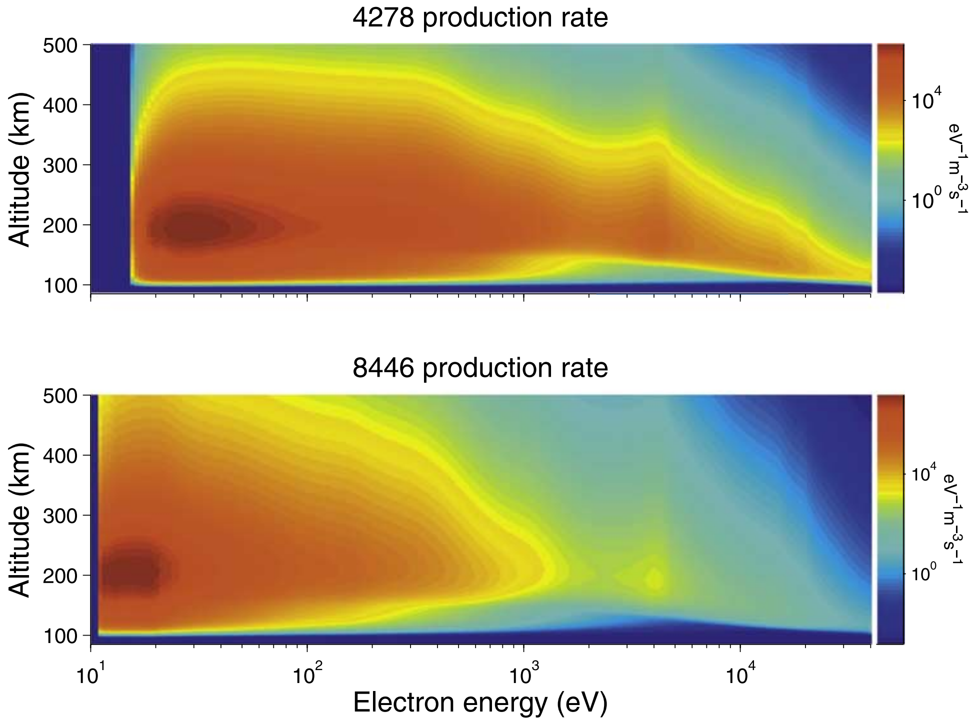

Figure 7. Altitude variation of the differential production rate of 4278 (top) and 8446 Å (bottom) for the electron flux at 21:34 UT.

Rees [1989]. The column emission rate at 4278 and 8446 Å we calculate with

$$I_{4278} = 10^{-6} \int_0^\infty n_{N_2} \int_0^\infty \sigma_4(E) I(E,s) dE ds \tag{3}$$

where σ_4 is the 4278 Å emission cross section of *Shaw and Campos* [1983] and $I(E, s) = I^d(E, s) + I^u(E, s)$; and

$$I_{8446} = 10^{-6} \int_0^\infty n_O \int_0^\infty \sigma_3(E) I(E,s) dE ds \tag{4}$$

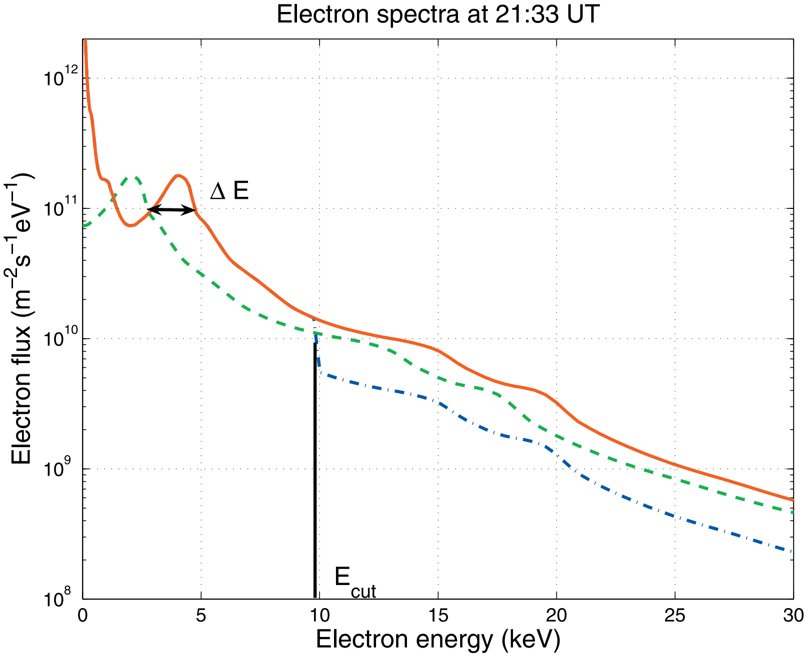

Figure 8. EISCAT estimate of the precipitating electron spectrum for 21:33:30 UT (red solid curve), the electron spectrum modified by a retarding potential ΔE (green dashed curve), and the electron spectrum affected by reduced pitch angle scattering at energies above E_{cut} (blue dot-dashed curve).

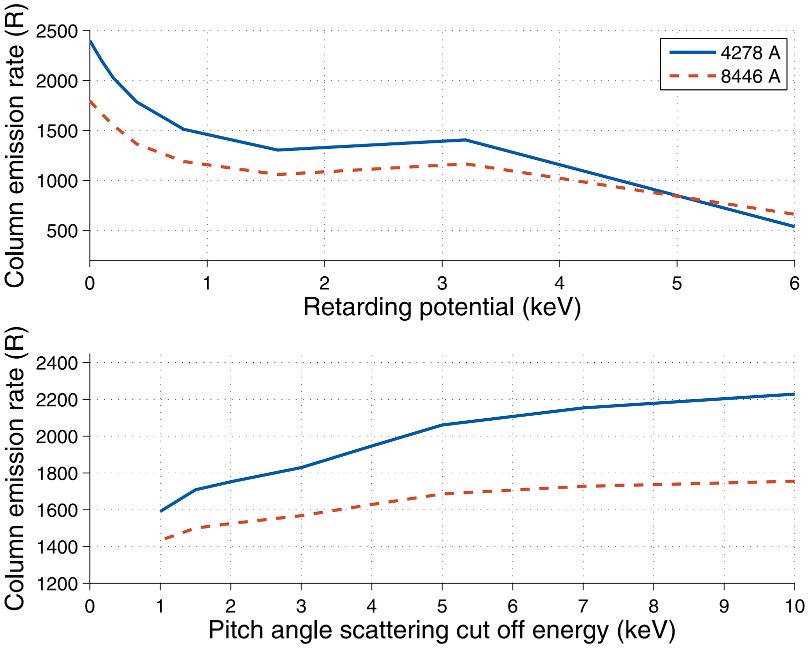

Figure 9. Reduction in column emission rates from 2400 R in 4278 and 1900 R in 8446 Å as a function of a low altitude retarding potential ΔE (top). Variation in 4278 and 8446 Å column emission rates as a function of a 67 percent reduction of electron flux above the cut-off energy E_{cut} (bottom).

where σ_3 is the O($3p^3P$) cross section from *Gulcicek and Doering* [1988].

[16] To model the effect of a retarding potential we simply reduce the energy of the primary spectra by ΔE. This we do for retarding potentials from 100 eV to 6.4 keV in steps of a factor of 2. To model the effect of reduced pitch angle scattering for high energy electrons we reduce the flux above a cut-off energy E_{cut} by 67 percent, which is approximately the reduction observed by *Peticolas et al.* [2002]. This is illustrated in Figure 8.

[17] The effect of the retarding potential on the optical emissions, shown in Figure 9, is a reduction of 4278 Å by 20–25 percent for a retarding potential ΔE of $\approx$1 keV, which is in good agreement with the FREJA observations by *Marklund et al.* [1997]. However, there is also a significantly larger relative reduction in the column emission rate for 8446 Å, which is reduced by 35% for the same potential. This is not consistent with our observations, which showed a greater reduction for 4278 than 8446 Å.

[18] For the partial double loss cone model, a cut-off energy of 3–4 keV leads to a 20–25 percent reduction in 4278 Å and a 10–15 percent reduction in 8446 Å, which is in good agreement with the FAST observations of *Peticolas et al.* [2002]. This is in good agreement with our observations.

[19] There is a contribution to 8446 Å from cascading of O($3s'^3D$) to O($3p^3P$). Since the optical depth for the 989 Å emission from O($3s'^3D$) is large, spatial structures in the electron excitation of in the O($3s'^3D$) will be smeared by scattering and absorption of 989 Å photons. According to *Christensen et al.* [1983] the contribution to 8446 Å is typically 27% in night side observations. This will contribute to a background intensity that is not affected by small-scale structures in the electron precipitation. This we have taken into account by adding a fixed background corresponding to 27% of the intensity in the diffuse aurora, to the modeled 8446 Å emissions.

[20] Finally, it should be noted that the altitude variation of the column emission rates in the dark structures will be different for the two models. Since the retarding potential mainly reduces the fluxes at lower energies, emissions at higher altitudes would be reduced more compared to the partially double loss cone model where it is the flux of high energy electrons that are reduced—leading to a reduction of volume emission rates at lower altitudes.

4. Summary and Conclusion

[21] We have presented the first combined incoherent scatter radar, bistatic white-light and monostatic spectral image observations of black aurora. We find that the black auroral structures have a reduction by approximately 25% in 4278 Å and 18% at 8446 Å compared to the intensities in the surrounding diffuse aurora, i.e., black aurora are not completely devoid of optical emissions. EISCAT measurements of electron density give us estimates of primary electron spectra that we use to model the optical emissions at 4278 and 8446 Å. The modeling shows that a retarding potential leads to a significantly larger relative reduction in the column emission rate of 8446 Å from atomic oxygen than 4278 Å from N_2^+, which is incompatible with our observations. This shows that a retarding potential at low altitudes is not what causes unsheared black aurora. Since the partial double loss cone model [*Peticolas et al.*, 2002] gives a better fit to our data, this indicates that unsheared black aurora are magnetopsheric regions of suppressed pitch angle scattering that drift with the gradient-B-curvature drift of trapped particles *Blixt et al.* [2005b]. The question is then: what causes the transition to the sheared black aurora [e.g., *Trondsen and Cogger*, 1997; *Kimball and Hallinan*,

1998b] where a downward E-field [*Marklund et al.*, 1997] creates the positive space charge that sustains any of the processes thought to cause the shear [*Johnson and Chang*, 1995; *Shukla et al.*, 1995; *Keskinen and Ganguli*, 1996]. To answer this question more combined radar-optical observations of diffuse aurora are needed preferably with simultaneous in situ observations of precipitating particles and electric fields.

[22] **Acknowledgments.** EISCAT is funded and by the research councils of Norway, Sweden, Finland, Japan, China, the United Kingdom and Germany. The authors thank the referees for their valuable comments.

[23] Wolfgang Baumjohann thanks Gerhard Haerendel and Dirk Lummerzheim for their assistance in evaluating this paper.

References

Blixt, E. M., and M. J. Kosch (2004), Coordinated optical and EISCAT observations of black aurora, *Geophys. Res. Lett.*, *31*, L06813, doi:10.1029/2003GL019244.

Blixt, E. M., T. Grydeland, N. Ivchenko, T. Hagfors, C. La Hoz, B. S. Lanchester, U. P. Løvhaug, and T. S. Trondsen (2005a), Dynamic rayed aurora and enhanced ion-acoustic radar echoes, *Ann. Geophys.*, *23*, 3–11.

Blixt, E. M., M. J. Kosch, and J. Semeter (2005b), Relative drift between black aurora and the ionospheric plasma, *Ann. Geophys.*, *23*, 1611–1621.

Brändström, B. U. E. (2003), The auroral large imaging system - design, operation and scientific results, Ph.D. thesis, Sci. Report 279, Swedish Inst. of Space Phys., Kiruna, Sweden.

Christensen, A. B., G. G. Sivjee, and J. H. Hecht (1983), OI (7990 Å) emission and radiative entrapment of auroral EUV, *J. Geophys. Res.*, *88*, 4911–4917.

Gulcicek, E. E., and J. P. Doering (1988), Absolute differential and integral electron excitation cross sections for atomic oxygen. Part V: Revised values for the $^3P \rightarrow {}^3S0$ (1304 Å) and $^3P \rightarrow {}^3D0$ (989 Å) transitions below 30 eV, *J. Geophys. Res.*, *93*, 5879–5884.

Hedin, A. (1991), Extension of the MSIS thermospheric model into the middle and lower atmosphere, *J. Geophys. Res.*, *96*, 1159–1172.

Johnson, J. R., and T. Chang (1995), Nonlinear vortex structures with diverging electric fields and their relation to the black aurora, *Geophys. Res. Lett.*, *22*, 1481–1484.

Keskinen, M. J., and G. Ganguli (1996), Simulation of dynamics and structure in the black aurora, *J. Geophys. Res.*, *101*, 26,995–26,999.

Kimball, J., and T. J. Hallinan (1998a), Observations of black auroral patches and of their relationship to other types of aurora, *J. Geophys. Res.*, *103*, 14,671–14,682.

Kimball, J., and T. J. Hallinan (1998b), A morphological study of black vortex streets, *J. Geophys. Res.*, *103*, 14,683–14,695.

Kosch, M., T. Hagfors, and E. Nielsen (1998a), A new digital all-sky imager experiment for optical auroral studies in conjunction with the Scandinavian twin auroral radar experiment, *Rev. Sci. Instrum.*, *69*, 578–584.

Kosch, M. J., M. J. W. Scourfield, and E. Nielsen (1998b), A self-consistent explanation for a plasma flow vortex associated with the brightening of an auroral arc, *J. Geophys. Res.*, *103*, 29,383–29,391.

Marklund, G., L. Blomberg, C.-G. Falthammar, and P.-A. Lindqvist (1994), On intense diverging electric fields associated with black aurora, *Geophys. Res. Lett.*, *21*, 1859–1862.

Marklund, G., T. Karlsson, and J. Clemmons (1997), On low-altitude particle acceleration and intense electric fields and their relationship to black aurora, *J. Geophys. Res.*, *102*, 17,509–17,522.

Oguti, T. (1975), Metamorphoses of aurora, *Mem. Natl. Inst. Polar Res. Ser. A.*, *101*, 1–101.

Peticolas, L. M., T. J. Hallinan, H. C. Stenbaek-Nielsen, J. W. Bonnell, and C. W. Carlson (2002), A study of black aurora from aircraft-based optical observations and plasma measurements on FAST, *J. Geophys. Res.*, *107*(A8), 1217, doi:10.1029/2001JA900157.

Porter, H. S., F. Varosi, and H. G. Mayr (1987), Iterative solution of the multistream electron transport equation: 1. Comparison with laboratory beam injection experiments, *J. Geophys. Res.*, *92*, 5933–5959.

Rees, M. H. (1989), *Physics and Chemistry of the Upper Atmosphere*, Cambridge Univ. Press, New York.

Rishbeth, H., and A. van Eyken (1993), EISCAT: Early history and the first ten years of operation, *J. Atmos. Sol. Terr. Phys*, *55*, 525–542.

Royrvik, O. (1976), Pulsating aurora: Local and global morphology, Ph.D. thesis, Univ. of Alaska, Fairbanks.

Schoute-Vanneck, H., M. W. J. Scourfield, and E. Nielsen (1990), Drifting black aurora?, *J. Geophys. Res.*, *95*, 241–246.

Semeter, J., and F. Kamalabadi (2005), Determination of primary electron spectra from incoherent scatter radar measurements of the auroral E region, *Radio Sci.*, 40, RS2006, doi:10.1029/2004RS003042.

Shaw, M., and J. Campos (1983), Emission cross sections of the second positive and first negative systems of N_2 and N_2^+ excited by electron impact, *J. Quant. Spectrosc. Radiat. Transfer*, *30*, 73–76.

Shukla, P. K., G. T. Birk, and R. Bingham (1995), Vortex streets driven by sheared flow and applications to black aurora, *Geophys. Res. Lett.*, *22*, 671–674.

Solomon, S. C., P. B. Hays, and V. J. Abreu (1988), The auroral 6300 Å emission: Observation and modelling, *J. Geophys. Res.*, *93*, 9867–9882.

Stamnes, K. (1981), On the two-stream approach to electron transport and thermalization, *J. Geophys. Res.*, *86*, 2405–2410.

Swartz, W. E., J. S. Nisbet, and A. E. S. Green (1971), Analytic expression for the energy-transfer rate from photoelectrons to thermal electrons., *J. Geophys. Res.*, *76*, 8425–8426.

Trondsen, T. S., and L. L. Cogger (1997), High-resolution television observations of black aurora, *J. Geophys. Res.*, *102*, 363–378.

Turunen, T., A. Westman, I. Häggström, and G. Wannberg (2002), High resolution general purpose d-layer experiment for EISCAT incoherent scatter radars using selected set of random codes, *Ann. Geophys.*, *20*, 1469–1477.

E. M. Blixt and B. Gustavsson, Department of Physics and Technology, University of Tromsø, N-9037 Tromsø, Norway. (marten.blixt@gmail.com; bjorn.gustavsson@phys.uit.no)

B. U. E. Brändström, Kiruna Division, Swedish Institute of Space Physics, Box 812, SE-981 28 Kiruna, Sweden.

A. J. Kavanagh, M. J. Kosch, and A. Senior, Department of Communication Systems, InfoLab21, Lancaster University, Lancaster, LA1 4WA UK. (mkosch@ lancs.ac.uk)